

Visualization of Local Conductance in MoS₂/WSe₂ Heterostructure Transistors

Di Wu^{1†}, Wei Li^{2†}, Amritesh Rai², Xiaoyu Wu¹, Hema C. P. Movva², Maruthi N. Yogeesh²,
Zhaodong Chu¹, Sanjay K. Banerjee², Deji Akinwande², Keji Lai^{1*}

¹ Department of Physics, The University of Texas at Austin, Austin, TX 78712, United States

² Microelectronics Research Center, Department of Electrical and Computer Engineering, The University of Texas at Austin, Austin, TX 78758, United States

[†] DW and WL contributed equally to this work.

* E-mail: kejilai@physics.utexas.edu

Abstract

The vertical stacking of van der Waals (vdW) materials introduces a new degree of freedom to the research of two-dimensional (2D) systems. The interlayer coupling strongly influences the band structure of the heterostructures, resulting in novel properties that can be utilized for electronic and optoelectronic applications. Based on microwave microscopy studies, we report quantitative electrical imaging on gated molybdenum disulfide (MoS_2)/tungsten diselenide (WSe_2) heterostructure devices, which exhibit an intriguing antiambipolar effect in the transfer characteristics. Interestingly, in the region with significant source-drain current, electrons in the n-type MoS_2 and holes in the p-type WSe_2 segments are nearly balanced, whereas the heterostructure area is depleted of mobile charges. The spatial evolution of local conductance can be ascribed to the lateral band bending and formation of depletion regions along the line of MoS_2 –heterostructure– WSe_2 . Our work vividly demonstrates the microscopic origin of novel transport behaviors, which is important for the vibrant field of vdW heterojunction research.

Keywords: van der Waals heterostructure, microwave impedance microscopy (MIM), antiambipolar effect, band alignment, depletion region.

Van der Waals (vdW) heterostructures (HSs) with atomically sharp interfaces and controllable layer components have been intensively investigated in the past few years¹⁻⁵. The interlayer vdW coupling, although much weaker than the intralayer covalent bonding, is sufficient to modify the band structures of the assembled materials. For instance, when two disparate semiconducting transition-metal dichalcogenide (TMDC) layers are stacked together, the energy band offset⁶ may strongly influence the carrier dynamics⁷⁻¹⁶ and transport characteristics¹⁷⁻²⁷. Due to the atomically thin nature of few-layer TMDCs, the depletion region in the vertical direction across the heterojunction, which is ubiquitously found in heterojunctions of three-dimensional (3D) semiconductors, does not exist in such 2D systems¹⁹. Taking advantage of these new features, researchers have demonstrated novel electronic and optoelectronic devices such as heterojunction photodiodes¹⁷⁻²⁰, resonant/Esaki tunneling diodes²¹⁻²³, multivalued logic inverters²⁴, electron-hole multiplication photocells²⁷, floating-gate memories²⁸, and excitonic transistors²⁹. It is anticipated that the research in vdW heterostructures will continue to thrive in the foreseeable future.

Among the various TMDC heterostructures, the combination of MoS₂ and WSe₂ has received a lot of attention^{9,10,13,15,17-19,21-26,28-30}. Due to the presence of S vacancies and strong metal Fermi-level pinning near its conduction band edge, MoS₂ usually exhibits n-type characteristics³¹⁻³³. WSe₂, while being ambipolar, is mostly used as a p-type semiconductor because of its high hole mobility^{34,35}. The subsequent formation of p-n junctions and the type-II band alignment with large band offsets⁶ have led to interesting phenomena such as band-to-band tunneling^{22,24,26}, negative differential resistance^{22,24,30}, and ultra-long valley lifetime¹⁵, among others. On the other hand, transport and most optical measurements are inherently macroscopic in nature and the sample response is averaged over large areas. In this work, we report the electrical mapping of a gated MoS₂/WSe₂ heterostructure transistor by microwave impedance microscopy (MIM)³⁶. Transport across the device during the electrostatic gating shows a clear antiambipolar behavior^{19,22-24}, which was also observed in other heterostructure systems³⁷⁻³⁹. Interestingly, while the local conductance of individual MoS₂ and WSe₂ layers exhibits the usual n-type and p-type behavior, respectively, the heterostructure area is fully depleted of free carriers when an appreciable source-drain current can flow through the device. We show that such a counterintuitive spatial evolution of electrical conductance can be described by the band bending model and the presence of lateral depletion regions. Our work elucidates the underlying microscopic properties of vdW heterojunction devices, which is highly desirable for the continuous advance of 2D heterostructure research.

The TMDC HSs in this work were prepared by stacking exfoliated few-layer MoS₂ and WSe₂ flakes onto SiO₂ (300 nm)/Si substrates using a hot pick-up technique with polypropylene carbonate (PPC)-coated polydimethylsiloxane (PDMS) stamps^{40,41}. After the assembly, the samples were annealed in vacuum at 300 °C to improve the interlayer coupling. Details of the HS preparation steps are found in the Methods section. Metal electrodes on the TMDC flakes, 20 nm Pd/ 30 nm Au on WSe₂ and 5 nm Ti/ 45 nm Au on MoS₂, were patterned by standard electron-beam lithography, electron-beam evaporation and lift-off techniques (see Methods section). Quasi-Ohmic contacts were formed at the metal-TMDC interface at room temperature, as confirmed by the linear current-voltage (I-V) characteristics on individual materials (Supporting Information S1). For the experiment presented here, we do not observe any dependence on the stacking order between MoS₂ and WSe₂.

Fig. 1a shows the optical image of a typical MoS₂/WSe₂ transistor device with metal contacts. As seen from the atomic-force microscopy image and the line profile in Fig. 1b, both the MoS₂ and WSe₂ flakes are around 2 nm in thickness, corresponding to 3 monolayers. The samples are sufficiently thin such that the depletion region in the vertical direction is negligible²⁴. We therefore do not expect qualitative difference between our devices and thinner TMDC samples. The positions of the characteristic Raman peaks on individual flakes as well as the HS overlap region (Fig. 1c) are consistent with that reported in the literature^{26,42,43}. The transfer and output characteristics of the HS device are plotted in Fig. 1d and 1e, respectively. As the back-gate voltage V_{BG} increases from a very negative value of -20 V, the source-drain current (I_{DS}), starting from a negligible value, rises at $V_{BG} = -15$ V, peaks at around $V_{BG} = -10$ V, and drops back to the off state beyond $V_{BG} = 0$ V. In this work, such an unusual antiambipolar behavior is seen in all MoS₂/WSe₂ devices (Supporting Information S2). The same effect was reported in the literature^{19,22-24} and has been attributed to the lateral tunneling of carriers across the HS transistor. However, the underlying spatial distribution of electrical conductance in such HS transistors has not been studied in previous reports. Finally, upon further increase of V_{BG} , I_{DS} rises again since the current can now flow through the n-type MoS₂ and the n-branch of the ambipolar WSe₂^{23,24}.

The gate-dependent local conductance of the MoS₂/WSe₂ transistor was studied by a microwave impedance microscope (MIM)³⁶ based on a tuning fork (TF) atomic-force microscope (AFM)^{44,45}. As illustrated in Fig. 2a, an electrochemically etched tungsten tip with a diameter

around 100 nm, which sets the spatial resolution of the technique, is attached to a quartz TF for topographic feedback. The MIM signal, modulated by the TF resonant frequency (~ 32 kHz), is demodulated by a lock-in amplifier to form the AC_MIM image. Details of the TF-based MIM and the driving-amplitude-modulation (DAM) feedback mode are found in Ref. 45. The sample thickness measured by the TF-AFM is the same as that determined by conventional contact-mode AFM (Supporting Information S3). During the experiment, the source and drain electrodes are grounded and the DC offset of the tip is set to be zero through a bias-tee such that the tip does not behave as a top gate on the sample.

In Fig. 2b, the I_{DS} - V_{BG} curve around the antiambipolar peak at a small V_{DS} of 0.3 V is replotted in the linear scale and divided into three distinct transport regimes (regions I, II and III corresponding to different V_{BG} ranges). For simplicity, we only present selected AC_MIM-Im (proportional to the imaginary component of the tip-sample admittance) data, which are monotonic as a function of the local conductance (see analysis below) in Fig. 2c. The complete set of MIM images are included in Supporting Information S4. On individual TMDC flakes, the MIM signals gradually increase (decrease) with increasing V_{BG} on the MoS₂ (WSe₂) part of the device. In contrast, the MIM signals on the HS overlap area display a non-monotonic gate dependence, which can be divided into three regions in accordance with the transfer curve of Fig. 2b. Being conductive at $V_{BG} = -20$ V, the HS gradually turns resistive with increasing V_{BG} within Region I, starting from the MoS₂-HS boundary and moving inward. In the antiambipolar Region II (-15 V $< V_{BG} < -2.5$ V), the MIM signals on the HS area are essentially the same as that on the substrate, indicative of an insulating behavior. For further increase of V_{BG} in Region III, conductivity reappears inside the HS, again starting from the MoS₂ side and moving toward the interior. The non-uniform MIM signals along the left edge of the HS area are presumably due to local defects and variation in the interlayer coupling. At a very positive $V_{BG} = 20$ V, the HS area is uniformly conductive except for a dark line on the right side, possibly due to the folding of flakes. Note that the MIM signal here is slightly lower than that on the highly conductive MoS₂. The same evolution of AC_MIM data are also observed in other MoS₂/WSe₂ devices in this study (Supporting Information S5).

For a quantitative understanding of the MIM data, we have performed finite-element analysis (FEA) of the tip-sample interaction⁴⁶ using commercial software COMSOL 4.4. Details of the geometric and electrical parameters for the simulation are shown in Supporting Information

S6. For the TF-based MIM, the tip-sample admittance is first simulated as a function of the tip height. As the tip taps on the sample surface, the admittance oscillates at the same TF resonant frequency. The first harmonic signal obtained by Fourier transform of the time-domain simulation curve then corresponds to the MIM data acquired by the lock-in amplifier. Fig. 3a shows the simulated AC_MIM signal with respect to the 2D sheet conductance σ_{sh} , which is indeed a monotonically increasing function in the relevant regime of $10^{-8} \text{ S/m} < \sigma_{sh} < 10^{-5} \text{ S/m}$. A comparison between the FEA result and the measured data in Fig. 3b allows us to quantitatively extract the average sheet conductance, as plotted in Fig. 3c. We emphasize that the gate dependence of local conductance in this HS device is nontrivial. In particular, the HS area is highly insulating in Region II where the trans-conductance is significant. The resistance between the source and drain electrodes is, therefore, not the summation of the resistances of the three segments, as is expected in a simple series circuit.

The counterintuitive local sheet conductance imaged by the MIM can be understood by the lateral band alignment across the device. With strong interlayer coupling, the overlap area of the HS device can be viewed as a new TMDC material, whose energy bands are hybridized from MoS₂ and WSe₂. While band bending in the vertical direction is absent in few-layer TMDC materials, the drift and diffusion of free carriers will still lead to band bending in the horizontal direction and the formation of depletion regions. The lateral band alignment across the three segments at zero source-drain bias is qualitatively illustrated in Fig. 4a. In Region I with highly negative V_{BG} , the MoS₂, HS, WSe₂ areas are depleted, weakly p-type, and strongly p-type, respectively. As V_{BG} increases and the Fermi level E_F rises, depletion region inside the HS first appears near the MoS₂ side and gradually moves towards the interior of the HS. Note that the lateral width of this insulating section is small at the left and right corners of the HS area, where the two individual TMDC layers are in close proximity. As the device is forward biased ($V_{DS} > 0 \text{ V}$) and the potential barrier in the HS lowered, the recombination current will flow mainly through these corners rather than having to traverse the center of the HS. The resultant output characteristics are similar to that of the traditional p-n junction diode (see Fig. 1e), except that a significant forward current only occurs when both the p-WSe₂ and n-MoS₂ regions are sufficiently conductive around $V_{BG} = -12 \text{ V}$. As V_{BG} further increases, MoS₂ becomes heavily n-doped and WSe₂ is depleted. Carriers can no longer travel across the device and the transport current drops again. For even higher V_{BG} , it is

expected that WSe₂ also becomes n-doped and I_{DS} increases again. The fact that the WSe₂ region remains insulating at $V_{BG} = 20$ V may be due to certain surface electrochemistry, which can be mitigated by a capping layer in future work. The evolution of local conductance in the middle of the HS area is vividly seen in the line profiles plotted in Fig. 4b. The gradual change of MIM signals along the line of MoS₂-HS-WSe₂ indicates that the band bending occurs in a length scale of $0.5 \sim 1$ μm . Such information is not accessible through transport studies and can only be obtained by the electrical mapping in our MIM measurements.

In summary, we demonstrate the quantitative electrical imaging of few-layer MoS₂/WSe₂ heterostructure transistors by microwave impedance microscopy. The local sheet conductance on the n-type MoS₂ and p-type WSe₂ sections of the device changes monotonically as a function of the back-gate voltage. The heterostructure area, on the other hand, is depleted of free carriers in the middle of the antiambipolar region where the transport current can flow through the device. The gate dependence of local conductance evolution can be satisfactorily explained by the lateral band alignment model. Since nanoscale conductivity is an essential property for electronic applications, our spatial mapping of the local conductance is of crucial importance for the rapid progress of vdW heterostructure research.

Methods

Van der Waals heterostructure preparation: Few-layer MoS₂ and WSe₂ flakes were first mechanically exfoliated onto SiO₂ (300 nm)/Si substrates using Scotch tape and Gel-Pak film, and then annealed at 300 °C in vacuum (base pressure $\sim 10^{-6}$ Torr) for 6 h to remove tape residues. The flake thicknesses were determined using atomic-force microscopy (AFM) measurements and were found to be ~ 2 nm for both MoS₂ and WSe₂. The heterostructures were assembled by stacking one MoS₂ flake onto another WSe₂ flake using a hot dry-transfer pick-up technique with polypropylene carbonate (PPC)-coated polydimethylsiloxane (PDMS) stamps. A flake of MoS₂ was first picked up by the PDMS/PPC stamp at 40 °C and then stacked onto another WSe₂ flake on the target SiO₂ (300 nm)/Si substrate at 110 °C. The high temperature enabled delamination and release of the PPC film onto the target substrate, and was critical to reduce the trapped moisture

and gases in the heterostructure interface region. After the PPC was released, the target substrate was soaked in chloroform, acetone and isopropanol consecutively to remove the PPC residue. The heterostructure samples were then annealed in vacuum at 300 °C to improve the interface quality in order to enhance the interlayer coupling.

Device fabrication and transport measurement: Metal contacts were deposited via electron-beam evaporation (base pressure $\sim 5 \times 10^{-6}$ Torr) after the electrode regions were defined by conventional electron-beam lithography utilizing poly(methyl methacrylate) (PMMA) as the resist. Different metals were chosen to form low resistance quasi-Ohmic contacts with different TMDC flakes at room temperature: 20 nm Pd/30 nm Au was deposited as contacts for WSe₂ and 5 nm Ti/45 nm Au was deposited as contacts for MoS₂. After the contact lift-off in acetone, the surface of the heterostructure flakes was further cleaned by contact-mode AFM scanning before the MIM and transport measurements. The transport measurements were carried out in the dark using Keithley 4200 and 4201 Semiconductor Characterization Systems (SCS) under ambient conditions.

MIM measurements: A tuning-fork-based MIM was employed to map the local conductance. In particular, an electrochemically etched tungsten tip was attached to a quartz tuning fork (resonant frequency ~ 32 kHz). A Zurich HF2L1 lock-in amplifier was used to control the tuning-fork tip to vibrate at its resonant frequency in the driving amplitude modulation (DAM) mode⁴⁵. The topography feedback system was provided by a commercial AFM system (Park XE-70). The AC_MIM signals were demodulated by a SR830 lock-in amplifier and then acquired by the Park AFM system. During the measurements, source and drain electrodes were grounded, and the back-gate voltage was applied using a Keithley 2400 Source Measure Unit (SMU) to modulate the carrier density.

Finite-element analysis (FEA): Finite-element analysis by COMSOL 4.4 was carried out to quantify the sheet conductance of TMDC flakes. Since the lateral dimensions of the flakes are much larger than the MIM tip diameter, the 2D axisymmetric model can be used here. Details of the geometric and electrical parameters are found in Supporting Information S4. We then follow the standard procedure in Ref. 45 to convert the demodulated tip-sample admittance to the AC_MIM output based on the calibration of our electronics. Note that the AC_MIM signal is plotted as a function of the 2D sheet conductance $\sigma_{\text{sh}} = \sigma_{3\text{D}} \cdot t$, where $\sigma_{3\text{D}}$ is the 3D conductivity

and t is the flake thickness. Since t is much smaller than the tip diameter, the MIM response of MoS₂, HS, WSe₂ segments follows the same simulation curve shown in Fig. 3a.

Acknowledgments

The MIM experiment was supported by the U.S. Department of Energy (DOE), Office of Science, Basic Energy Sciences, under the Awards No. DE-SC0010308 and DE-SC0019025. The sample fabrication was supported by the Welch Foundation Grant No. F-1814. D.A. acknowledges the Presidential Early Career Award for Scientists and Engineers (PECASE). This work was partly done at the Microelectronics Research Center (MRC) of the Texas Nanofabrication Facility, a member of the National Nanotechnology Coordinated Infrastructure (NNCI) supported by the National Science Foundation (NSF) grant ECCS-1542159 as well as the Multidisciplinary University Research Initiative (MURI) grant W911NF-17-1-0312. A.R. and S.K.B. would also like to acknowledge support from the NASCENT Engineering Research Center (ERC) funded by NSF grant EEC-1160494.

Supporting Information

Additional details on transport and microwave imaging results of other heterostructure devices, as well as finite-element analysis. This material is available free of charge via the Internet at <http://pubs.acs.org>.

Author Contributions

K.L. conceived the project. D.W. and W.L. fabricated the devices and performed the transport measurements. A.R., H.C.P.M. and M.N.Y. assisted with the heterostructure preparation. D.W. conducted the MIM experiments, performed data analysis and drafted the manuscript with K.L. All authors have contributed to the manuscript preparation and have given approval to the final version of the manuscript.

Conflict of Interest

The authors declare no competing financial interest.

References

1. A. K. Geim and I. V. Grigorieva, “Van der Waals heterostructures”, *Nature* **499**, 419 (2013).
2. M.-Y. Li, C.-H. Chen, Y. Shi, and L.-J. Li, “Heterostructures based on two-dimensional layered materials and their potential applications”, *Mater. Today* **19**, 322 (2016).
3. Chaoliang Tan, Zhuangchai Lai, and Hua Zhang, “Ultrathin Two-Dimensional Multinary Layered Metal Chalcogenide Nanomaterials”, *Adv. Mater.* **29**, 1701392 (2017).
4. Chaoliang Tan, Xiehong Cao, Xue-Jun Wu, Qiyuan He, Jian Yang, Xiao Zhang, Junze Chen, Wei Zhao, Shikui Han, Gwang-Hyeon Nam, Melinda Sindoro, and Hua Zhang, “Recent Advances in Ultrathin Two-Dimensional Nanomaterials”, *Chem. Rev.* **117**, 6225 (2017).
5. Xiao Zhang, Zhuangchai Lai, Qinglang Ma, and Hua Zhang, “Novel structured transition metaldichalcogenide nanosheets”, *Chem. Soc. Rev.* **47**, 3301 (2018).
6. J. Kang, S. Tongay, J. Zhou, J. Li, and J. Wu, “Band offsets and heterostructures of two-dimensional semiconductors”, *Appl. Phys. Lett.* **102**, 012111 (2013).
7. X. Hong, J. Kim, S.-F. Shi, Y. Zhang, C. Jin, Y. Sun, S. Tongay, J. Wu, Y. Zhang, and F. Wang, “Ultrafast charge transfer in atomically thin MoS₂/WS₂ heterostructures”, *Nat. Nanotech.* **9**, 682 (2014).
8. H. Heo, J. H. Sung, S. Cha, B.-G. Jang, J.-Y. Kim, G. Jin, D. Lee, J.-H. Ahn, M.-J. Lee, J. H. Shim, H. Choi, and M.-H. Jo, “Interlayer orientation-dependent light absorption and emission in monolayer semiconductor stacks”, *Nat. Commun.* **6**, 7372 (2014).
9. M.-H. Chiu, M.-Y. Li, W. Zhang, W.-T. Hsu, W.-H. Chang, M. Terrones, H. Terrones, and L.-J. Li, “Spectroscopic Signatures for Interlayer Coupling in MoS₂-WSe₂ van der Waals Stacking”, *ACS Nano* **8**, 9649 (2014).
10. H. Fang, C. Battaglia, C. Carraro, S. Nemsak, B. Ozdol, J. S. Kang, H. A. Bechtel, S. B. Desai, Fl. Kronast, A. A. Unal, G. Conti, Ca. Conlon, G. K. Palsson, M. C. Martin, A. M. Minor, C. S. Fadley, E. Yablonovitch, R. Maboudian, and A. Javey, “Strong interlayer coupling in van der Waals heterostructures built from single-layer chalcogenides”, *Proc. Natl. Acad. Sci.* **111**, 6198 (2014).
11. P. Rivera, J. R. Schaibley, A. M. Jones, J. S. Ross, S. Wu, G. Aivazian, P. Klement, K. Seyler, G. Clark, N. J. Ghimire, J. Yan, D.G. Mandrus, W. Yao, and X. Xu, “Observation

- of long-lived interlayer excitons in monolayer MoSe₂–WSe₂ heterostructures”, *Nat. Commun.* **6**, 6242 (2015).
12. D. Kozawa, A. Carvalho, I. Verzhbitskiy, F. Giustiniano, Y. Miyauchi, S. Mouri, A. H. Castro Neto, K. Matsuda, and G. Eda, “Evidence for Fast Interlayer Energy Transfer in MoSe₂/WS₂ Heterostructures”, *Nano Lett.* **16**, 4087 (2016).
 13. O. L. Sanchez, D. Ovchinnikov, S. Misra, A. Allain, and A. Kis, “Valley Polarization by Spin Injection in a Light-Emitting van der Waals Heterojunction”, *Nano Lett.* **16**, 5792 (2016).
 14. J. S. Ross, P. Rivera, J. Schaibley, E. Lee-Wong, H. Yu, T. Taniguchi, K. Watanabe, J. Yan, D. Mandrus, D. Cobden, W. Yao, and X. Xu, “Interlayer Exciton Optoelectronics in a 2D Heterostructure p–n Junction”, *Nano Lett.* **17**, 638 (2017).
 15. J. Kim, C. Jin, B. Chen, H. Cai, T. Zhao, P. Lee, S. Kahn, K. Watanabe, T. Taniguchi, S. Tongay, M. F. Crommie, and F. Wang, “Observation of ultralong valley lifetime in WSe₂/MoS₂ heterostructures”, *Sci. Adv.* **3**, e1700518 (2017).
 16. C. Jin, E. Y. Ma, O. Karni, E.C. Regan, F. Wang, and T. F. Heinz, “Ultrafast dynamics in van der Waals heterostructures”, *Nat. Nanotech.* **13**, 994 (2018).
 17. M. M. Furchi, A. Pospischil, F. Libisch, J. Burgdörfer, and T. Mueller, “Photovoltaic Effect in an Electrically Tunable van der Waals Heterojunction”, *Nano Lett.* **14**, 4785 (2014).
 18. R. Cheng, D. Li, H. Zhou, C. Wang, A. Yin, S. Jiang, Y. Liu, Y. Chen, Y. Huang, and X. Duan, “Electroluminescence and Photocurrent Generation from Atomically Sharp WSe₂/MoS₂ Heterojunction p–n Diodes”, *Nano Lett.* **14**, 5590 (2014).
 19. C.-H. Lee, G.-H. Lee, A. M. van der Zande, W. Chen, Y. Li, M. Han, X. Cui, G. Arefe, C. Nuckolls, T. F. Heinz, J. Guo, J. Hone, and P. Kim, “Atomically thin p–n junctions with van der Waals heterointerfaces”, *Nat. Nanotech.* **9**, 676 (2014).
 20. N. Flory, A. Jain, P. Bharadwaj, M. Parzefall, T. Taniguchi, K. Watanabe, and L. Novotny, “A WSe₂/MoSe₂ heterostructure photovoltaic device”, *Appl. Phys. Lett.* **107**, 123106 (2015).
 21. Y.-C. Lin, R. K. Ghosh, R. Addou, N. Lu, S. M. Eichfeld, H. Zhu, M.-Y. Li, X. Peng, M. J. Kim, L.-J. Li, R. M. Wallace, S. Datta, J. A. Robinson, “Atomically thin resonant tunnel diodes built from synthetic van der Waals heterostructures”, *Nat. Commun.* **6**, 7311 (2015).

22. T. Roy, M. Tosun, X. Cao, H. Fang, D.-H. Lien, P. Zhao, Y.-Z. Chen, Y.-L. Chueh, J. Guo, and A. Javey, “Dual-Gated MoS₂-WSe₂ van der Waals tunnel diodes and Transistors”, *ACS Nano* **9**, 2071 (2015).
23. N. Huo, S. Tongay, W. Guo, R. Li, C. Fan, F. Lu, J. Yang, B. Li, Y. Li, and Z. Wei, “Novel Optical and Electrical Transport Properties in Atomically Thin WSe₂/MoS₂ p–n Heterostructures”, *Adv. Electron. Mater.* **1**, 1400066 (2015).
24. A. Nourbakhsh, A. Zubair, M. S. Dresselhaus, and T. Palacios, “Transport Properties of a MoS₂/WSe₂ Heterojunction Transistor and Its Potential for Application”, *Nano Lett.* **16**, 1359 (2016).
25. C. Li, X. Yan, X. Song, W. Bao, S. Ding, D. W. Zhang, and P. Zhou, “WSe₂/MoS₂ and MoTe₂/SnSe₂ van der Waals heterostructure transistors with different band alignment”, *Nanotechnology* **28**, 415201 (2017).
26. M.-H. Doan, Y. Jin, S. Adhikari, S. Lee, J. Zhao, S. C. Lim, and Y. H. Lee, “Charge Transport in MoS₂/WSe₂ van der Waals Heterostructure with Tunable Inversion Layer”, *ACS Nano* **11**, 3832 (2017).
27. F. Barati, M. Grossnickle, S. Su, R. K. Lake, V. Aji, and N. M. Gabor, “Hot carrier-enhanced interlayer electron–hole pair multiplication in 2D semiconductor heterostructure photocells”, *Nat. Nanotech.* **12**, 1134 (2017).
28. C. Liu, X. Yan, X. Song, S. Ding, D. W. Zhang, and P. Zhou, “A semi-floating gate memory based on van der Waals heterostructures for quasi-non-volatile applications”, *Nat. Nanotech.* **13**, 404 (2018).
29. D. Unuchek, A. Ciarrocchi, A. Avsar, K. Watanabe, T. Taniguchi, and A. Kis, “Room-temperature electrical control of exciton flux in a van der Waals heterostructure”, *Nature* **560**, 340 (2018).
30. Hema C. P. Movva, Sangwoo Kang, Amritesh Rai, Kyoungwan Kim, Babak Fallahazad, Takashi Tanig, Kenji Watanabe, Emanuel Tutuc, and Sanjay K. Banerjee, “Room temperature gate-tunable negative differential resistance in MoS₂/hBN/WSe₂ heterostructures”, 74th Annual Device Research Conference (DRC), 2016, pp 1–2.
31. B. Radisavljevic, A. Radenovic, J. Brivio, V. Giacometti, and A. Kis, “Single-layer MoS₂ transistors”, *Nat. Nanotech.* **6**, 147 (2011)

32. Amritesh Rai, Hema C. P. Movva, Anupam Roy, Deepyanti Taneja, Sayema Chowdhury, and Sanjay K. Banerjee, “Progress in contact, doping and mobility engineering of MoS₂: An atomically thin 2D semiconductor”, *Crystals* **8**, 316 (2018).
33. Amritesh Rai, Amithraj Valsaraj, Hema C.P. Movva, Anupam Roy, Rudresh Ghosh, Sushant Sonde, Sangwoo Kang, Jiwon Chang, Tanuj Trivedi, Rik Dey, Samaresh Guchhait, Stefano Larentis, Leonard F. Register, Emanuel Tutuc, and Sanjay K. Banerjee, “Air stable doping and intrinsic mobility enhancement in monolayer molybdenum disulfide by amorphous titanium suboxide encapsulation”, *Nano Lett.* **15**, 4329 (2015)
34. Hema C. P. Movva, Amritesh Rai, Sangwoo Kang, Kyoungwan Kim, Babak Fallahazad, Takashi Taniguchi, Kenji Watanabe, Emanuel Tutuc, and Sanjay K. Banerjee, “ High-mobility holes in dual-gated WSe₂ field effect transistors”, *ACS Nano* **9**, 10402 (2015).
35. Babak Fallahazad, Hema C. P. Movva, Kyoungwan Kim, Stefano Larentis, Takashi Taniguchi, Kenji Watanabe, Sanjay K. Banerjee, and Emanuel Tutuc, “Shubnikov–de Haas oscillations of high-mobility holes in monolayer and bilayer WSe₂: Landau level degeneracy, effective mass, and negative compressibility”, *Phys. Rev. Lett.* **116**, 086601 (2016).
36. D. Wu, X. Li, L. Luan, X. Wu, W. Li, M. N. Yogeesh, R. Ghosh, Z. Chu, D. Akinwande, Q. Niu, and K. Lai, “Uncovering edge states and electrical inhomogeneity in MoS₂ field-effect transistors”, *Proc. Natl. Acad. Sci.* **113**, 8583 (2016).
37. Deep Jariwala, Vinod K. Sangwan, Chung-Chiang Wu, Pradyumna L. Prabhurashi, Michael L. Geier, Tobin J. Marks, Lincoln J. Lauhon, and Mark C. Hersam, “Gate-tunable carbon nanotube-MoS₂ heterojunction p-n diode”, *Proc. Natl. Acad. Sci.* **110**, 18076 (2013).
38. Deep Jariwala, Vinod K. Sangwan, Jung-Woo Ted Seo, Weichao Xu, Jeremy Smith, Chris H. Kim, Lincoln J. Lauhon, Tobin J. Marks, and Mark C. Hersam “Large-Area, Low-Voltage Antiambipolar Heterojunctions from Solution-Processed Semiconductors”, *Nano Lett.* **15**, 416 (2015).
39. Jaewoo Shim, Seyong Oh, Dong-Ho Kang, Seo-Hyeon Jo, Muhammad Hasnain Ali, Woo-Young Choi, Keun Heo, Jaeho Jeon, Sungjoo Lee, Minwoo Kim, Young Jae Song, and Jin-Hong Park, “Phosphorene/rhenium disulfide heterojunction-based negative differential resistance device for multi-valued logic”, *Nature Commun.* **7**, 13413 (2016).

40. Kyoungwan Kim, Matthew Yankowitz, Babak Fallahazad, Sangwoo Kang, Hema C. P. Movva, Shengqiang Huang, Stefano Larentis, Chris M. Corbet, Takashi Taniguchi, Kenji Watanabe, Sanjay K. Banerjee, Brian J. LeRoy, and Emanuel Tutuc, “van der Waals heterostructures with high accuracy rotational alignment”, *Nano Lett.* **16**, 1989 (2016).
41. F. Pizzocchero, L. Gammelgaard, B. S. Jessen, J. M. Caridad, L. Wang, J. Hone, P. Bøggild and T. J. Booth, “The hot pick-up technique for batch assembly of van der Waals heterostructures”, *Nat. Commun.* **7**, 11894 (2016).
42. Hong Li, Qing Zhang, Chin Chong Ray Yap, Beng Kang Tay, Teo Hang Tong Edwin, Aurelien Olivier, and Dominique Baillargeat, “From bulk to monolayer MoS₂ : Evolution of Raman scattering”, *Adv. Funct. Mater.* **22**, 1385 (2012).
43. Weijie Zhao, Zohreh Ghorannevis, Kiran Kumar Amara, Jing Ren Pang, Minglin Toh, Xin Zhang, Christian Kloc, Ping Heng Tane, and Goki Eda, “Lattice dynamics in mono- and few-layer sheets of WS₂ and WSe₂”, *Nanoscale* **5**, 9677 (2013)
44. Y.-T. Cui, E. Y. Ma, and Z.-X. Shen, “Quartz tuning fork based microwave impedance microscopy”, *Rev. Sci. Instrum.* **87**, 063711 (2016).
45. X. Wu, Z. Hao, D. Wu, L. Zheng, Z. Jiang, V. Ganesan, Y. Wang, and K. Lai, “Quantitative measurements of nanoscale permittivity and conductivity using tuning-fork-based microwave impedance microscopy”, *Rev. Sci. Instrum.* **89**, 043704 (2018).
46. K. Lai, W. Kundhikanjana, M. Kelly, Z.-X. Shen, “Modeling and characterization of a cantilever-based near-field scanning microwave impedance microscope”, *Rev. Sci. Instrum.* **79**, 06370 (2008).

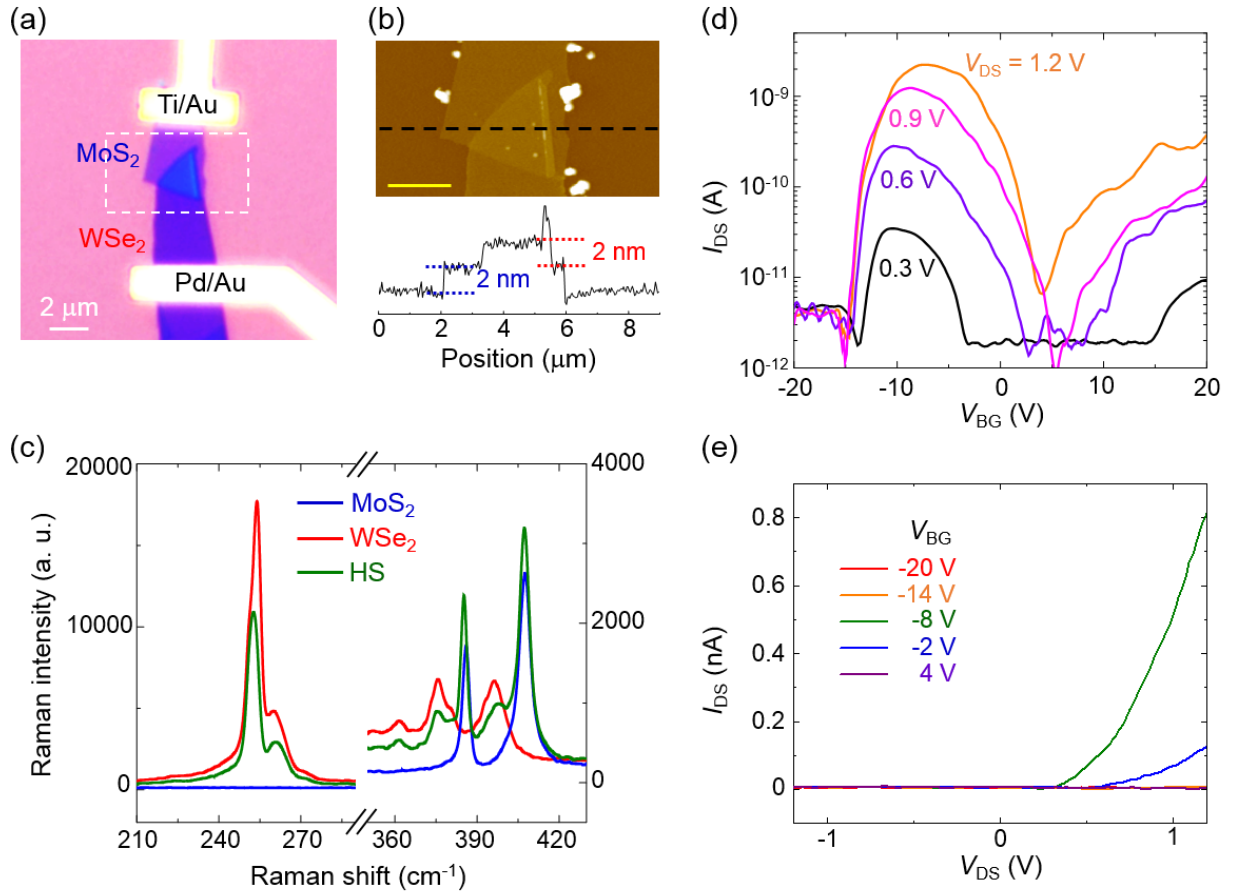


Figure 1. (a) Optical image of the MoS₂/WSe₂ heterostructure device with source (Ti/Au) and drain (Pd/Au) electrodes. (b) Top: AFM image inside the white dashed box in (a). The bright particles are tape residues. The scale bar is 2 μm . Bottom: line profile across the black dashed line in the AFM image, showing a thickness of 2 nm for both flakes. (c) Raman spectra acquired on three different locations of the sample with 532 nm excitation line. The heterostructure (HS) region displays characteristic Raman peaks of both MoS₂ and WSe₂. (d) Transfer characteristics of the HS transistor device under several source-drain biases. (e) Output characteristics of the device in (d) under several back-gate voltages.

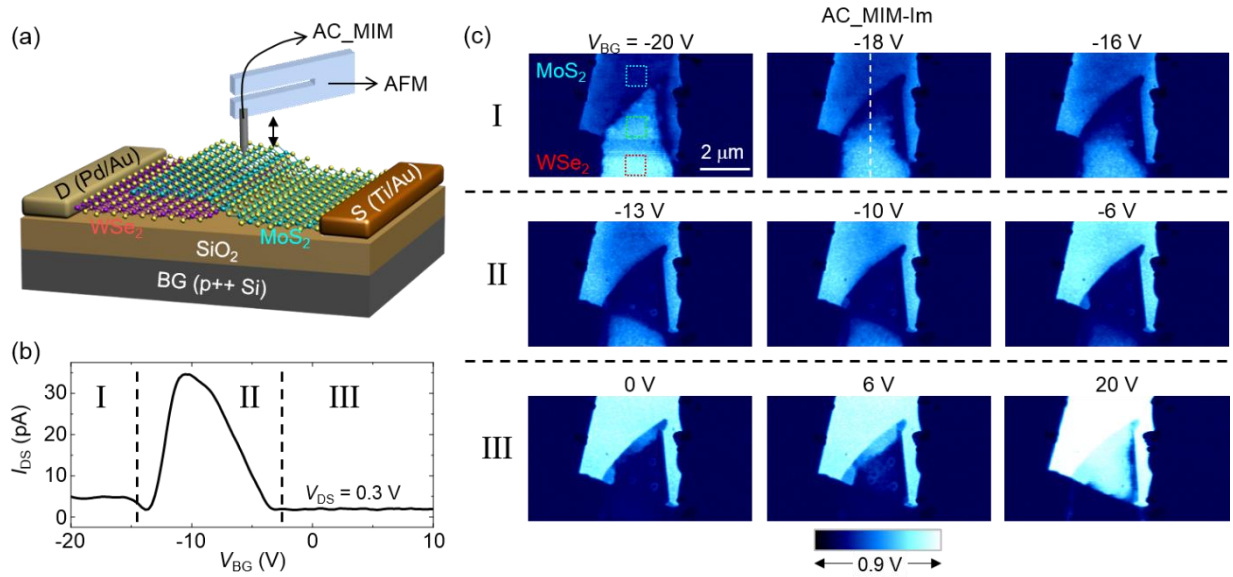


Figure 2. (a) Schematic of the experimental setup, showing the TF-based MIM and the heterostructure transistor. (b) Transfer curve at $V_{DS} = 0.3$ V. The two dashed lines roughly mark the three regions of the antiambipolar effect. (c) AC_MIM-Im images as a function of V_{BG} , separated into three regions according to the transport data. The field of view is the same as that in the AFM image of Fig. 1b.

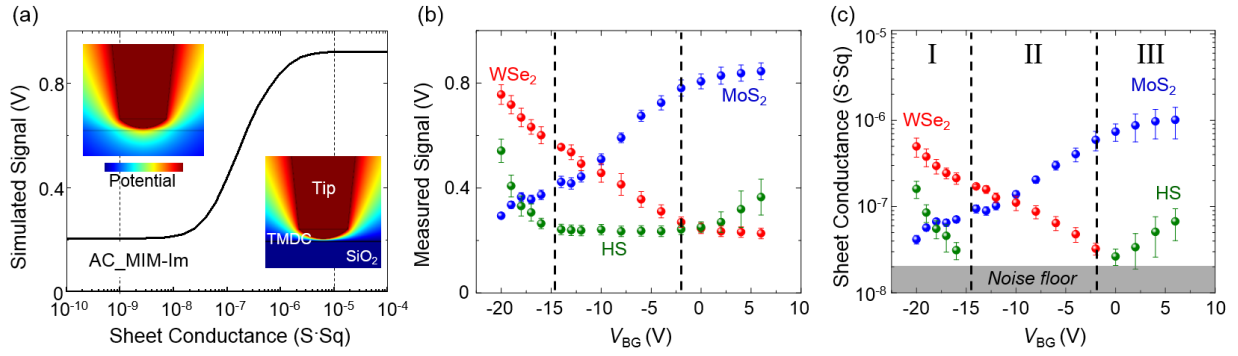


Figure 3. (a) Simulated AC_MIM-Im signal as a function of the 2D sheet conductance σ_{sh} . The insets show the quasi-static potential distribution at $\sigma_{sh} = 10^{-9}$ and 10^{-5} S·sq. (b) Averaged MIM signals inside the dashed squares (blue for MoS₂, green for HS, and red for WSe₂) in Fig. 2c. (c) Gate dependence of σ_{sh} extracted from (a) and (b). The dashed lines again mark the three regions in the transport data.

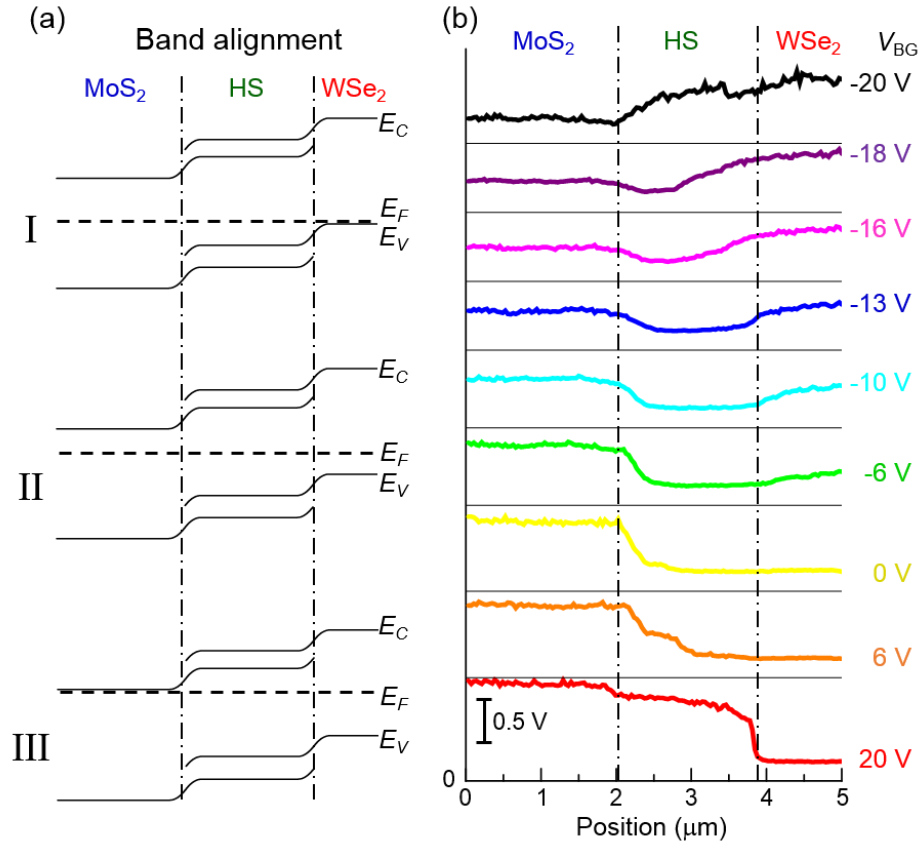


Figure 4. (a) Schematics of the lateral band alignment along the line of MoS₂-HS-WSe₂ in the three regions at $V_{DS} = 0$ V. E_C , E_F , and E_V represent the bottom of the conduction band, Fermi level, and the top of the valence band, respectively. (b) Selected MIM line profiles ($V_{DS} = 0$ V) along the white dashed line shown in the $V_{BG} = -18$ V image in Fig. 2c. The zero point baseline is shown at the bottom of each line profile. The gradual change of MIM signals in the length scale of $0.5 \mu\text{m}$ across the lateral junctions provides a measure of the depletion region width.